Shape-controlled self-assembly of light-powered microrobots into ordered microchains for cells transport and water remediation

Xia Peng[1], Mario Urso[1], Martina Ussia[1], Martin Pumera[1, 2, 3, 4 *]

[1] Future Energy and Innovation Laboratory, Central European Institute of Technology, Brno University of Technology, Purkynova 123, 61200, Brno, Czech Republic

[2] Center for Nanorobotics and Machine Intelligence, Department of Chemistry and Biochemistry, Mendel University in Brno, Zemedelska 1, 61300, Brno, Czech Republic

[3] Department of Medical Research, China Medical University Hospital, China Medical University, No. 91 Hsueh-Shih Road, Taichung, Taiwan, ROC

[4] Department of Chemical and Biomolecular Engineering, Yonsei University, 50 Yonsei-ro, Seodaemun-gu, 03722, Seoul, Korea

* Corresponding author e-mail: martin.pumera@ceitec.vutbr.cz

Keywords: micromotors; swarming; collective behavior; self-assembly; cargo transport; photo-Fenton degradation.

Abstract

Nature presents collective behavior of living organisms aiming to accomplish complex tasks, inspiring the development of cooperative micro/nanorobots. Herein, the spontaneous assembly of hematite-based microrobots with different shapes is presented. Autonomous motile light-driven hematite/Pt microrobots with cubic and walnut-like shapes are prepared by hydrothermal synthesis, followed by the deposition of a Pt layer to design Janus structures. Both microrobots show a fuel-free motion ability under light irradiation. Because of the asymmetric orientation of the dipolar moment in the crystal, cubic hematite/Pt microrobots can self-assemble into ordered microchains, contrary to the random aggregation observed for walnut-like microrobots. The microchains exhibit different synchronized motions under light irradiation depending on the mutual orientation of the individual microrobots during the assembly, which allow them to accomplish multiple tasks, including capturing, picking up and transporting microscale objects, such as yeast cells and suspended matter in water extracted from personal care products, as well as degrading polymeric materials. Such light-powered self-assembled microchains demonstrate an innovative cooperative behavior for small-scale multitasking artificial robotic systems, holding great potential toward cargo capture, transport and delivery, and wastewater remediation.

Introduction

Ranging from ant colonies to bird flocking, nature provides a plethora of intriguing collective phenomena in biological systems, self-assembled in a synchronized manner to accomplish desired tasks and goals that individual capabilities cannot achieve. For example, a colony of ants can cooperate based on achievable local information to transport food, construct nests, and self-assemble into sophisticated structures when encountering rugged terrain;[1] vast groups of starlings can twist, turn, swoop and swirl across the sky in beautiful shape-shifting clouds, known as starling murmuration, to scare and repel natural enemies. Such ingenious behaviors in the absence of any external influences exhibit superior advantages to complete tasks in a highly efficient and robust way, or survive in complex environments, fascinating researchers especially from the field of micro/nanorobotics. Inspired by the cooperative actions of living organisms, various artificial swarm robotic systems consisting of relatively simple robots have been developed, capable of complex task sequencing and communal formations relying on operator inputs or artificial intelligent software.[2, 3]

Artificial micro/nanorobots, a relatively young field of research that has seen remarkable growth, becoming one of the most attractive research topics nowadays, are autonomously self-propelled micro/nanomaterials able to harvest and convert energy from their surrounding environment into autonomous movement with distinct capabilities for accomplishing various tasks.[4, 5] Various energy sources, including chemical fuels (H_2O_2, glucose, urea) or external stimuli such as light, magnetic fields, and ultrasound, have been exploited to activate the self-propulsion of micro/nanorobots.[6–13] Particularly, light is a very attractive energy source to power microrobots because it is powerful, renewable, and abundant. To obtain an active

moving particle, it is necessary to have an asymmetric structure, which in turn converts this asymmetry into motion.[14, 15] In this regard, the "two-faced" Janus microrobots consisting of a photocatalytic semiconductor (UV-light-activated TiO_2 and ZnO, visible light-activated Fe_2O_3 and BiOI) asymmetrically covered by a metal layer (Pt, Au, Ag) represent the most efficient light-powered self-motile microrobots.[16–25] Owing to their powerful motion, micro/nanorobots can accomplish numerous and different tasks, holding excellent prospects in various application fields from biomedicine to environmental remediation and sensing.[26–29] Still, further improvements are expected from rudimentary communication between individual microrobots (e.g., micro/nanorobotic swarms), allowing synchronized operation and high adaptability to different complex conditions. Based on this consideration, the careful selection of the constituent materials plays a crucial role in micro/nanorobots' organization manners. In fact, self-propelled micro/nanorobots composed of colloids can exhibit swarm behaviors via physical or chemical interactions, such as dipole−dipole interactions, capillary forces, van der Waals forces, *etc.*, rather than informatic communication in macrorobotic systems.[30–36] For instance, Bi_2WO_6 microrobots presented swarms of multiple microrobots under continuous light exposure due to the release of ionic species.[37] Another case of microrobotic assembly is provided by peanut-shaped hematite colloids. With a combination of oscillating and rotating magnetic fields, swarms can be formed in the state of chains, vortices, and ribbons.[10] Similarly, helical swimmers consisting of polymeric helical structures covered with ferromagnetic thin films can be assembled into straight chains and various other configurations, such as bent chains, crosses, and more.[38] Furthermore, Au/Ru nanorods were forced by acoustic standing waves into various configurations, such as chains or rings.[39] Nevertheless, microrobots that

can self-assemble into microchains in the absence of any external influences with a reconfigurable capability and exhibit light-driven propulsion in a synchronized way with different motion modes remain to be explored.

In this work, we demonstrate the intriguing collective behavior of light-powered cubic hematite microrobots remarkably different from that of walnut-like hematite microrobots. (**Scheme 1**). The microrobots were fabricated by asymmetrically depositing a 30 nm thin Pt layer on the surface of walnut-like and cubic-shaped hematite microparticles synthesized by facile and low-cost hydrothermal processes. All microrobots show self-propulsion under UV-light irradiation in pure water. Cubic microrobots display faster locomotion than walnut-like ones, agreeing with the larger mixed potential differences observed from Tafel measurements.

Moreover, cubic hematite microrobots can self-assemble into impressive microchains exhibiting three types of autonomous motion under UV-light irradiation, according to the orientation of microrobots during the formation of the microchains. The self-assembled microchains can address multitasking requirements when encountering environmental variations, including capturing, picking up, and transporting micro-objects, such as cells and suspended matter in water resulting from the contamination with personal care products as photocatalytic degradation of polymer chains. This work offers self-assembled light-powered microchains based on dipolar interactions between individual cubic hematite/Pt Janus microrobot, which promise cargo transportation and degradation of pollutants in water, including plastic materials.

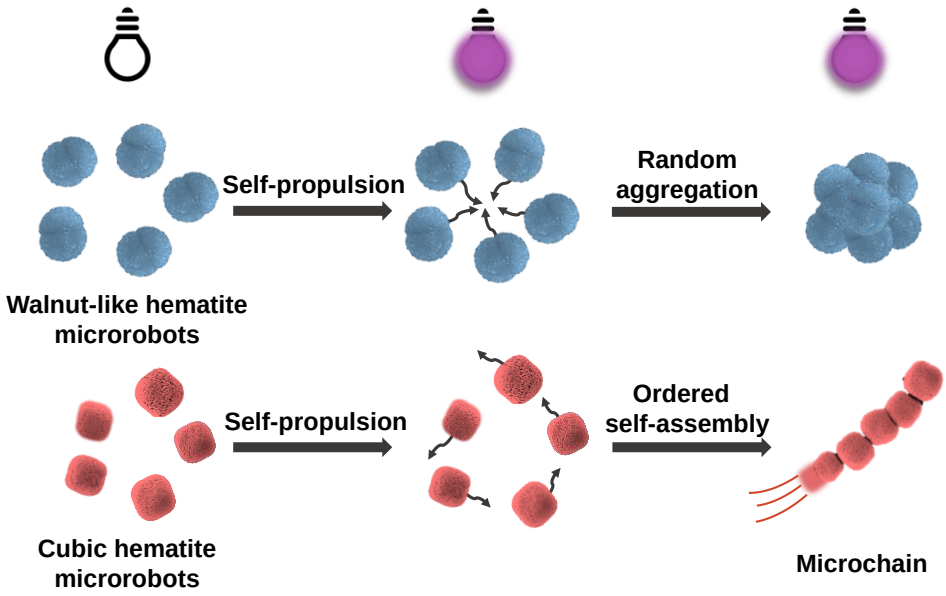

Scheme 1. Shape-controlled self-assembly capabilities of light-powered hematite/Pt Janus microrobots under UV-light irradiation.

Results and discussion

Janus Microrobots Fabrication

The different shapes of micro/nanorobots play a crucial role in their self-assembly or collective behaviors. In this work, we investigated the influence of microrobots' shape on their collective behaviour using self-propelled light-driven walnut-like and cubic hematite/Pt Janus microrobots.

As illustrated in **Figure 1a**, different shapes of hematite microparticles were first synthesized by facile hydrothermal reactions. To fabricate Janus microrobots, 30 nm Pt films were physically deposited on the surface of hematite microparticles by the sputtering method. Scanning electron microscopy (SEM) images and the corresponding elemental mapping images obtained by energy-dispersive X-ray spectroscopy (EDX) of the two hematite shapes are presented in **Figures 1b and c**. **Figure 1b** shows walnut-like hematite microparticles with a diameter of 2–3 μm and a hierarchical porous structure resulting from the random arrangement of hematite nanoparticles (approximately 100 nm). As shown in **Figure 1c**, hematite microcubes displayed a round-edged morphology and relatively rough surface with an average size of about 2 μm. EDX images manifest a uniform distribution of Fe and O for both hematite microparticles. After Pt layer deposition, both hematite microrobots exhibit the distinct asymmetrical structure of Janus microrobots, as indicated by the uneven Pt distribution.

X-ray diffraction (XRD) was carried out to assess hematite microparticles crystalline structure, as shown in **Figure S1**. The recorded XRD patterns correspond to the characteristic α-Fe_2O_3 pattern (PDF card # 00-001-1053). The peaks appearing at the following 2θ values ≈24.12°, 33.12°, 35.61°, 40.88°, 49.51°, 54.22°, 57.63°, 62.45°, and 64.11°, corresponds to

(012), (104), (110), (113), (024), (116), (018), (214), and (300) planes, respectively. These peaks agree with the distinctive rhombohedral centered hexagonal structure of the α-Fe_2O_3 crystal, commonly called hematite.[22]

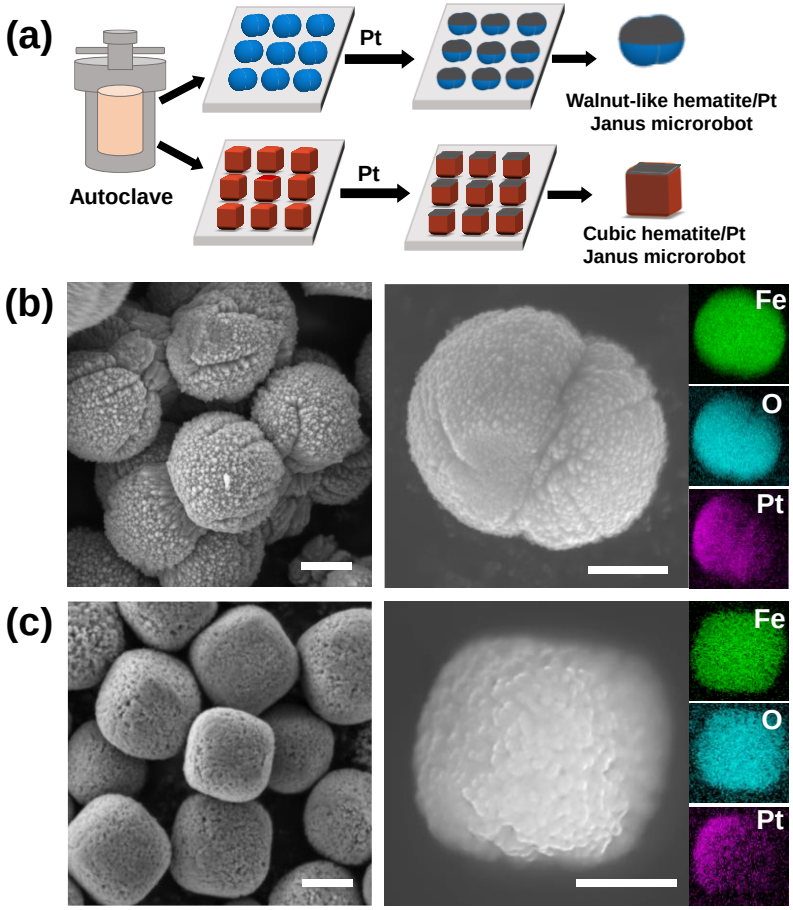

Figure 1. (a) Fabrication scheme of hematite/Pt Janus microrobots with different shapes. SEM and EDX elemental mapping images of (b) walnut-like and (c) cubic hematite/Pt Janus microrobots (scale bars are 1 μm).

Single Microrobots Propulsion

The hematite/Pt Janus microrobots displayed autonomous self-propelled abilities in water and low amounts of H_2O_2 fuel when irradiated with UV-light based on a light-induced self-

electrophoretic mechanism. Upon exposure to UV-light, charge separation occurs within hematite and electrons from the hematite conduction band are transferred to the Pt layer. Consequently, protons are produced at the hematite side from the oxidation of water and consumed at the Pt side, establishing a protons gradient. This generates an electroosmotic flow of water molecules, causing a net displacement of the particles and propelling the Janus microrobots with hematite as the forward side. [29] The addition of a small amount of H_2O_2 can result in a much stronger gradient of charges and more powerful propulsion, as illustrated in **Figure S2**. **Figure 2a** reports the speed of the walnut-like and cubic microrobots in different concentrations of H_2O_2, calculated from the average of more than 10 different microrobots. In pure water (0% H_2O_2), the speed of walnut-like microrobots (5 ± 1 μm s^{-1}) is slightly higher than cubic hematite microrobots (4.2 ± 0.8 μm s^{-1}). However, the addition of a small amount of H_2O_2 (0.1%) results in a huge increase in the speed of cubic hematite microrobots (19 ± 1 μm s^{-1}), while the speed of walnut-like ones is merely 6 ± 1 μm s^{-1}. **Figure 2b** shows the trajectories of walnut-like and cubic microrobots in 0.1% H_2O_2 under UV-light irradiation after 5 s recording, which demonstrate the much longer navigation within 5 s of the cubic ones (**Supplementary Movie 1**). When a higher concentration of H_2O_2 was applied (1% H_2O_2), there is an eight-fold increase in the speed of cubic microrobots (32 ± 3 μm s^{-1}) compared to pure water, while it is just tripled for walnut-like ones (14 ± 2 μm s^{-1}).

To better understand the underlying reasons for the differences in the speed of microrobots with different shapes, the mixed potential difference between walnut-like and cubic hematite microparticles and a Pt electrode was evaluated in 1% H_2O_2 under UV-light irradiation. According to previous work, [22, 25] a Tafel plot was used to obtain the potentials established at

different segments of the Janus microrobots (hematite and Pt) under UV-light illumination in H_2O_2. Tafel plots indicate that the variation in the mixed potentials between the electrodes is larger for cubic microrobots and consistent with the observed higher speed. As shown in **Figure 2c**, cubic hematite microrobots showed a more negative mixed potential under UV-light illumination than walnut-like hematite microrobots, indicating that more electrons migrate from cubic hematite electrode to Pt electrode. The potential difference between cubic hematite microparticles and Pt electrodes (47 mV) is much larger than walnut-like hematite (4 mV), consistently with the trend of microrobots' speed in **Figure 2a.** This phenomenon can be explained by the photoabsorption and charge transport properties of different faces in the hematite crystal structure. As evidenced by previous papers,[40, 41] it has demonstrated that (110) surface of hematite is more active than the (104) surface for photoelectrochemical. As shown in **Figure S1**, the normalized XRD pattern illustrated that the ratio of peaks corresponding to (110) and (104) faces for cubic hematite is larger than walnut-like hematite, which is consistent with the result of Tafel measurement.

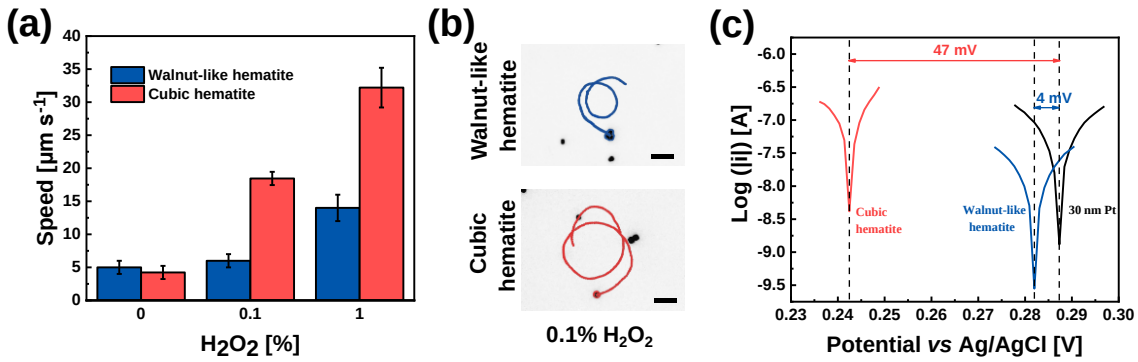

Figure 2. (a) Comparison of microrobots' speed in pure water and with different concentrations of H_2O_2. (b) Micrographs showing walnut-like and cubic microrobots trajectories in 0.1% H_2O_2 under UV-light

irradiation (scale bars are 5 μm). (c) Tafel plots of walnut-like and cubic hematite electrodes and 30 nm Pt electrode in 1% H_2O_2 under UV-light irradiation.

Collective Behaviour of Self-Assembled Microchains

We discovered that different microrobots' shapes give rise to different interactions. **Figure 3a** displays the temporal evolution of systems of walnut-like and cubic microrobots. In the beginning, walnut-like and cubic microrobots were randomly dispersed in water. After 10 min of observation, walnut-like microrobots displayed a random aggregation into large disordered clusters. As shown in **Figure S3a**, the direction of the dipolar moment is perpendicular to its long axis.[10] According to previous research, walnut-like hematite microrobots can assemble into chains cooperating with the magnetic field.[42] In contrast, only two-particle chains were found in the absence of a magnetic field, and mostly random aggregations were observed, as displayed in **Figure S3b**. Rod-shaped hematite microparticles with a long axis of approximately 1 μm and a short axis of approximately 500 nm were also fabricated to study their collective behavior without any external influence (**Figure S4a**). After 5min observation under the microscope in the absence of UV-light irradiation and H_2O_2, rod-shaped hematite microparticles formed random aggregates (**Figure S5a**), the same behavior as walnut-like hematite microparticles. On the contrary, cubic microrobots self-assembled into ordered microchains, which can be observed from optical microscopy and SEM. The live formation of the microchains is presented also in the **Supplementary Movie 2 and Supplementary Movie 3**, while several other microchains are reported in **Figure S6**. As SEM images shown in the **Figure S7**, we observed that cubic hematite microrobots self-assembled into microchains with

different lengths in pure water without UV-light irradiation. This intriguing phenomenon is due to the orientation of the dipolar moment in the crystal of cubic hematite, as illustrated **in Figure 3b**. For cubic hematite, the dipolar moment is not aligned along a particle symmetry axis. As explained in previous work,[43] the competing anisotropic interactions between the cube shape and dipole moment orientation are crucial for the formation of these remarkable microchains. Moreover, cubic hematite displays a fixed and permanent dipolar moment, even in the absence of a magnetic field, which is strong enough to induce the formation of self-assembled microchains.[44] It is worth noting that the presence of the Pt layer does not influence the active interaction between individual hematite microrobots, also as shown in **Figure S6 and Figure S7**. The length of the self-assembled microchains was measured both in dark and under UV-light irradiation and plotted as a function of the time, finding that it increases from 20 ± 3 μm to 100 ± 20 μm in dark and from 18 ± 4 μm to 80 ± 16 μm in the presence of UV-light when the time changes from 5 to 20 min (**Figure 3c**). We assumed that the light-induced motion of microrobots influence the formation of microchains to a certain degree, leading to shorter length under light irradiation. Based on these results, it can be concluded that the absence of external disturbances favors the self-assembly of the microrobots. Considering that reducing the size of cubic hematite particles may affect the self-assembly capability, nano-sized cubic hematite, whose size is reduced nearly four times compared to cubic hematite microparticles (**Figure S4b**), can self-assembled into microchains, as shown in **Figure S5b**, demonstrating that the permanent dipolar moment in the crystal structure is still strong enough to overcome the Brownian motion of nano-sized cubic hematite in water.

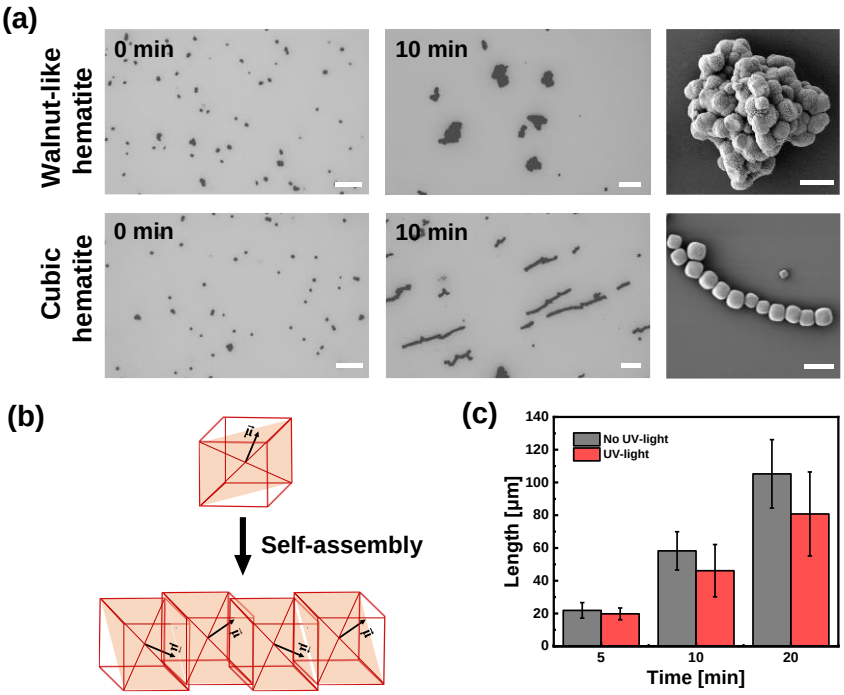

Figure 3. (a) Self-assembly of walnut-like and cubic microrobots in pure water in the absence of UV-light irradiation, and the corresponding SEM images after 10 min of observation (scale bars for SEM are 5 μm). (b) Dipolar moment orientation in a hematite cube and the alignment of a chain. (c) Length of the self-assembled microchains formed in pure water in the absence and presence of UV-light irradiation as a function of time.

The motion of the self-assembled microchains under UV-light irradiation was then investigated. The microchains exhibit three main motion modes in 0.1% H_2O_2 under UV-light irradiation, associated with a self-propulsion direction that is (1) parallel or (2) perpendicular to the microchain axis, or (3) a rotational behavior (**Supplementary Movie 4**). **Figure 4a** presents a series of time-lapse images, which illustrate the autonomous locomotion of microchains with the different propulsion modes.

The peculiar and varying motility of the microchains is ascribed to the distribution of the microrobots' Pt layers along the microchains, which depends on the microrobots' mutual

orientation during the self-assembly process. To corroborate this hypothesis, a numerical simulation of the 2D spatial distribution of H_2O resulting from the reaction between H_2O_2 and the photogenerated electrons transferred from hematite to Pt was conducted. In fact, this simulation provides an idea of the product spatial gradient which is responsible for microchains' self-propulsion. To simplify the calculation, a microchain formed by only two adjacent microrobots was considered. The different orientations of the Pt layer in the two microrobots give rise to different configurations, as shown in **Figure 4b**. In the configuration n. 1 and 2, the Pt layers are on the small side of the microchains. However, the configuration n. 1 results in the movement of the microchains along its axis, while the configuration n. 2 leads to a static microchain as the driving forces of the two microrobots are equal and oppositively directed. The configurations n. 3 and 4 are a combination of translation and rotation, while configuration n. 5 is responsible for the pure rotation of the microchain. Finally, the configuration n. 6 where the two Pt layer are adjacent and placed on the longer lateral side of the microchain enables the locomotion of the microchain along the direction perpendicular to its axis. It is important to point out that cubic hematite can arrange in longer macrochains. However, the chains with more than 3 cubes occur in hundreds of combinations making difficult their simulation and interpretation. Also, we believe that the propulsion behavior of longer microchains can be tracked back to the ideal two-particle microchains model. Unfortunately, these propulsion modes and the moving direction of microchains cannot be precisely controlled due to the random configuration of hematite microrobots and different orientations of their Pt layers during the self-assembly with or without UV-light irradiation.

Microchains also exhibited reconfigurable capability when an external magnetic field is

applied. First, the magnetic hysteresis loop of hematite microrobots was measured using a vibrating sample magnetometer (VSM). **Figure S8a** demonstrates that hematite microrobots exhibit ferromagnetic behavior. Then, the suspended solution of hematite microrobots was injected into a microfluidic channel. Time-lapse optical microscopy images in **Figure S8b**, captured from **Supplementary Movie 5**, illustrate that hematite microrobots rotated and moved towards the upside direction along the channel under a rotating magnetic field of 3 mT and 10 Hz, which resulted in the deformation of microchains. When the external magnetic field was removed, these microrobots spontaneously reconfigured into microchains. Such emerging collective behavior, leading to a synchronized motion of the microchains and reconfigurable capability are promising for completing tasks like the transport of cells or suspended matter as an example of possible contamination in water.

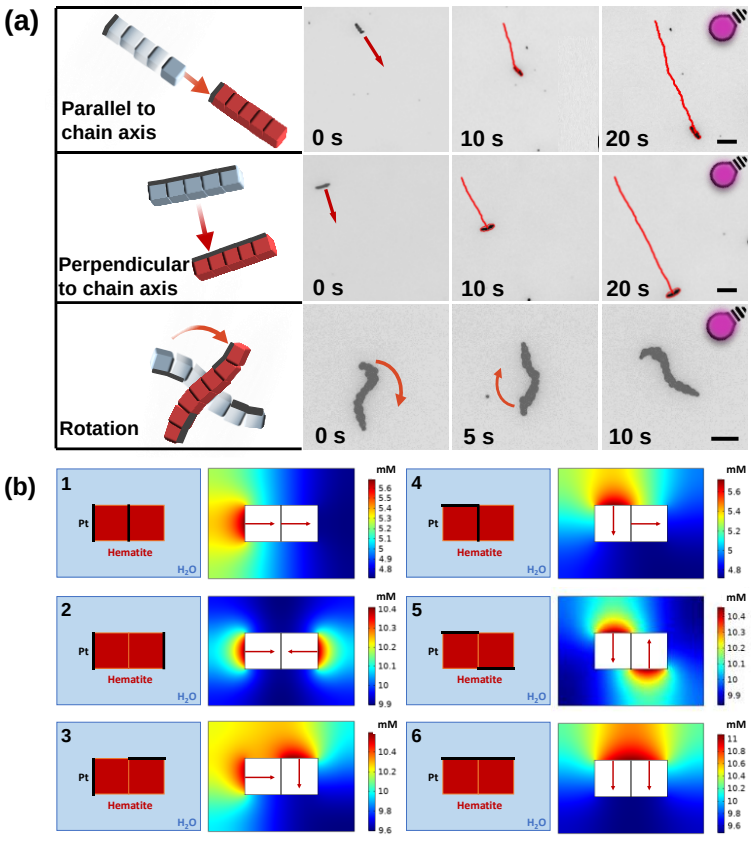

Figure 4. (a) Different motion modes of self-assembled microchains formed by cubic microrobots in 0.1% H_2O_2 under UV-light irradiation (Scale bars are 5 μm). (b) Simulation of 2D spatial distribution of H_2O resulting from the reaction between H_2O_2 and the photogenerated electrons transferred from hematite to Pt for different configurations of a 2-microrobots microchain. The arrows indicate the direction of the driving force.

Yeast cells capture, transport and release

Light-driven microrobots that can generate the local electric field and chemical gradients have demonstrated diverse interactions with surrounding passive particles, which is of great importance for performing desirable tasks such as cargo transport, objects manipulation, and sensing.[45–47] The self-assembly of cubic microrobots into autonomous motile microchains inspired their use for cargo transport application using yeast cells as a model for living microorganisms, owing to their relatively big size (approximately 2-3 μm for haploids) that can be easily visualized by optical microscopy. **Figure 5** displays the interaction between a cubic microrobot and yeast cells under UV-light irradiation in 0.1% H_2O_2 (**Supplementary Movie 6, 7**). The time-lapse images in **Figure 5a** demonstrate the long-distance transportation of a yeast cell by a single cubic microrobot. Besides, the rotation of multiple yeast cells can be realized by a single microrobot, as shown in **Figure 5b**. The transportation capability of self-assembled microchains were also evaluated. The self-assembled microchain in **Figure 5c** shows an autonomous motion parallel to the microchain axis, capturing four yeast cells, proving how the cooperation of several microrobots allows capturing and transporting several cells simultaneously in absence of magnetic field. We further investigated the controlled release of

yeast cells by switching on/off the UV-light in 0.1% H_2O_2 using the self-assembled microchains. As illustrated in **Figure 5d,** the microchain captured one yeast cell under UV-light irradiation owing to the photogenerated local chemical gradients and induced a phoretic attraction of the surrounding yeast cells. By turning off the UV-light, the yeast cell was immediately released, which is attributed to the hindered self-propulsion of the microchain and consequently the stopped generation of a chemical gradient around it. When UV-light was turned on again, the microchain produced photogenerated local chemical gradients, picked up again the yeast cell and continued to transport it.

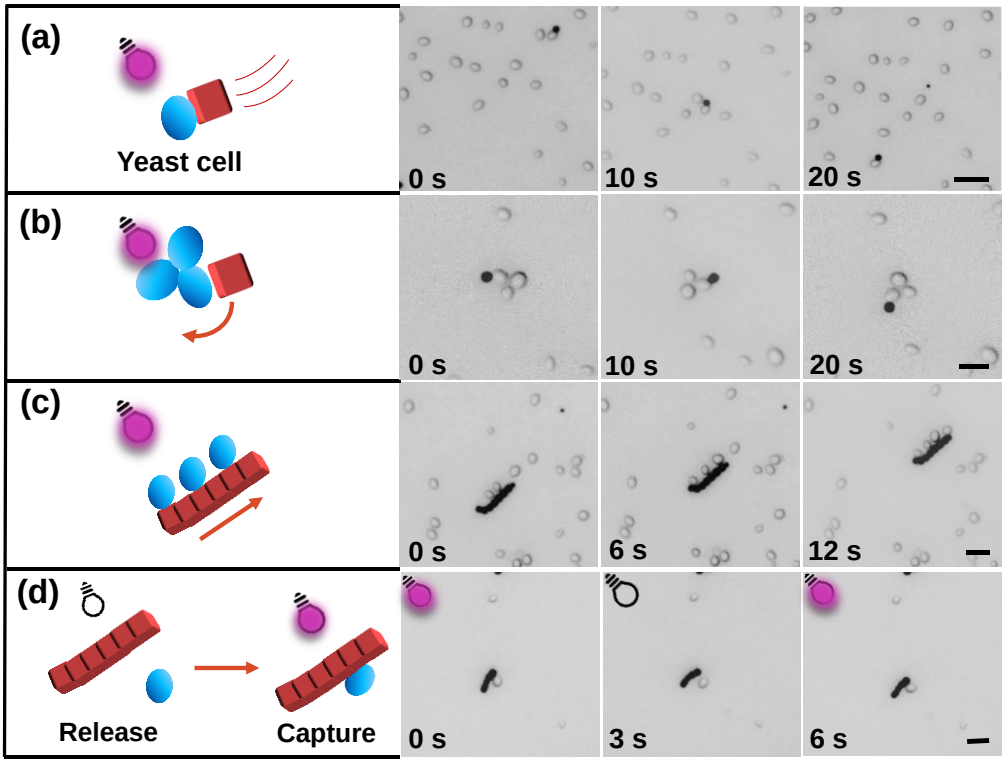

Figure 5. Interaction of cubic microrobots and self-assembled microchains with yeast cells in 0.1% H_2O_2 under UV-light irradiation. Time-lapse images of (a) a single microrobot transporting a yeast cell and (b) a single microrobot rotating with yeast cells, (c) a microchain capturing multiple yeast cells, and (d) controlled capture/release of the yeast cell by a microchain by turning on/off the UV-light (scale

bars are 5 μm).

Removal of suspended matter in water

Autonomous moving self-assembled microchains composed of synchronized microrobots open an opportunity to separate microplastics and suspended matter from water. The removal of suspended matter (**Figure S9**) extracted from commercial toothpaste was accomplished by the shoveling effect of microchains under UV-light irradiation in 0.1% H_2O_2 (**Supplementary Movie 8**). The artificially colored time-lapse images in **Figure 6a** (original images in **Figure S10**) demonstrate the motion of a microchain that was cleaning water by collecting suspended matter "on-the-fly." In fact, it can be observed that the removal area increases along the propulsion trajectory of the microchain, and within 60 s, a considerable number of pieces were quantitively accumulated on the forward side of the microchain, which further proves robust binding force between the single microrobots of the microchain. In comparison of other light-driven micromotors, most agents can exhibit swarming behavior in a random aggregation form under light irradiation,[37, 48] rather than regular microchains, which shows superior capability towards removal of microplastics.[49] Furthermore, hematite intrinsic magnetism without any surface functionalization can be used to navigate the microchains with captured microplastics using an external magnetic field, completing the remediation process. In addition to precise wireless positioning using an external magnetic field, microchains can also be navigated to regions difficult to access, such as the industrial tubes that are hard to reach with conventional strategies, providing an alternative solution for environmental applications in the future.[49, 50]

PEG photodegradation

To demonstrate the ability of the self-assembled microchains to degrade pollutants in water, the PEG 4000 has been chosen as a model for polymeric materials like plastics whose degradation can be monitored by Matrix-Assisted Laser Desorption/Ionization Mass Spectrometry (MALDI-MS). A higher concentration of H_2O_2 (1% H_2O_2) was employed in this experiment to exploit a higher self-propulsion speed and enhanced photocatalytic activity required to break the strong covalent bonds in polymer chains. Previous research has demonstrated that the concentrations of 1% H_2O_2 decreased from 10 000 ppm to less than 2 ppm after 24 h long treatment with hematite microrobots, which is lower than 8 ppm, the allowed limit of H_2O_2 in drinking water. Consequently, it can be concluded that H_2O_2 does not introduce new pollution in water system.[22] The sample was exposed to UV-light irradiation for 24 h in the presence of the cubic microrobots leading to the self-assembled microchains. **Figure 6b** reports MALDI spectra of bare PEG and microrobots-treated PEG solution. Signals corresponding to PEG macromolecular chains around 4000 mass completely disappeared after the treatment with microchains upon exposure to UV-light and H_2O_2, which is attributed to the combination of photocatalysis and catalyzed photo-Fenton reaction producing photogenerated ROS to attack C–O bonds in PEG backbone.[51] Several control experiments were performed to corroborate the effectiveness of the chain-like structure towards the degradation of PEG. It is worth noting that cubic hematite can form microchains under motion and no-motion conditions, i.e., with or without exposure to UV-light. Thus, it is difficult to establish the contribution of the microchains formation in this specific case. Due to this, PEG was treated with 1% H_2O_2 and UV-light irradiation separately and in combination to exclude secondary

effects during the photodegradation process. As it is possible to appreciate in **Figure S11**, it is clearly shown that PEG treated with UV-light and H_2O_2 separately remained stable or only partially degraded after 24 h of treatment. While, when UV-light and H_2O_2 were applied in combination, the PEG photodegradation was notable but significantly lower than for cubic hematite microchains. In agreement with previous studies about photodegradation of PEG mediated by microrobots, it is possible to conclude that the photo-Fenton reaction due to the simultaneous presence of iron-based microstructures, UV-light, and H_2O_2 is more effective.[22] On the other hand, as already discussed before and as evidenced in **Figure S6**, the hematite microcubes are able to self-assemble into microchains both with/without UV-light and in the absence or presence of H_2O_2. Thus, it is not possible to compare their photodegradation abilities with the single microrobots. Nevertheless, we retain that single microrobots can spontaneously aggregate without peculiar configurations in contaminated water solutions, thus partially reducing the surface area available and making difficult to understand the different performances between single or aggregated systems.[52]

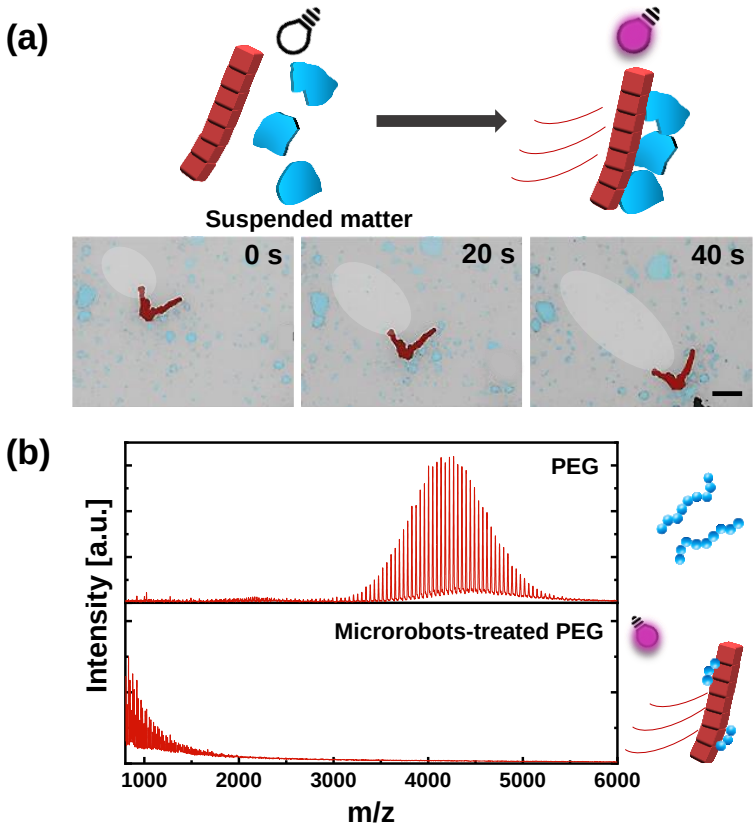

Figure 6. (a) Artificially colored time-lapse images of a self-assembled microchain for the removal of suspended matter under UV-light irradiation in 0.1% H_2O_2 (the white circles represent the area of suspended matter removal, blue areas are suspended matter pieces, red areas are microchains. The scale bar is 5 μm). (b) PEG chains photodegradation. From top to bottom, MALDI-MS of untreated PEG and PEG treated with microchains under 24 h UV-light irradiation in 1% H_2O_2.

Conclusion

In summary, we have demonstrated the influence of hematite/Pt microrobots shapes on their self-assembly behaviors. Because of the asymmetrical dipolar moment orientation in the crystal, cubic hematite/Pt microrobots can self-assemble into regular microchains with morphologies remarkably different from those of walnut-like microrobots, which solely display random aggregation. Taking advantage of the intriguing collective behavior, we also developed a light-

powered microchains composed of individual cubic hematite/Pt microrobots, exhibiting autonomous locomotion under UV-light irradiation in presence of low concentration of H_2O_2. These microchains demonstrate different types of self-propulsion depending on the various possible mutual orientations of the microrobots during the self-assembly, as well as reconfigurable capability after external magnetic field was employed to break the formation of self-assemble chains. To prove the exceptional benefits of a collective behavior compared to individual microrobot, these light-powered self-assembled microchains were employed for yeast cells capture, release and transport, for the capture and removal of suspended matter in water originated from personal care products, as well as the definitive degradation of polymeric materials. This work offers a different perspective on the collective behavior of photocatalytic microrobots with the benefits of easily batch fabrication, low-cost, and broad range of multimodal applications.

Experimental section

Synthesis of walnut-like hematite microparticles: Walnut-like hematite microparticles were prepared by a one-step hydrothermal reaction. In brief, 1 M $FeCl_3$ (Alfa Aesar, 98%) was added to deionized water (DI water, 18 MΩ cm) to form a homogeneous solution under magnetic stirring. Then the solution was transferred into a 50 mL Teflon-lined stainless-steel autoclave, heated at 160°C for 20 h, and cooled to room temperature naturally. Afterward, the product was collected by centrifugation and washed several times with DI water and ethanol. Finally, it was dried in a vacuum oven at 60°C for 12 h.

Synthesis of cubic-shaped hematite particles: For cubic hematite microparticles, in a typical synthesis, 0.5 M $FeCl_3$ (Alfa Aesar, 98%) and 1.2 g hexamethylenetetramine (Sigma Aldrich, 99.5%) were directly dissolved in a 30 mL mixture of ethanol and DI water (1:1 v/v) with vigorous magnetic stirring. Subsequently, 3 wt% of $CuCl_3$ (Alfa Aesar, 98%) was added to the above solution. After 30 min stirring, the mixture was transferred into a Teflon-lined stainless-steel autoclave and heated at 160℃ for 12 h. After that, the autoclave was cooled naturally down to room temperature. The resultant precipitate was collected by centrifugation, washed several times with DI water and ethanol, and then dried at 80℃ in a vacuum oven for 8h. For nano-sized cubic hematite, 0.5 M $FeCl_3$ (Alfa Aesar, 98%) and 1.2 g hexamethylenetetramine (Sigma Aldrich, 99.5%) were directly dissolved in a 30 mL mixture of ethanol and DI water (1:1 v/v) with vigorous magnetic stirring. After 30 min stirring, the mixture was transferred into a Teflon-lined stainless-steel autoclave and heated at 160℃ for 10 h. After that, the autoclave was cooled naturally down to room temperature. The resultant precipitate was collected by centrifugation, washed several times with DI water and ethanol, and then dried at 80℃ in a vacuum oven for 8 h.

Synthesis of rod-shape hematite microparticles: An NaOH solution (90 ml of 6 *N*) was added to 100 ml of well-stirred 2 M $FeCl_3$ solution in a 200 ml Pyrex bottle during 5 min, followed by the addition of 10 ml of 0.6 M Na_2SO_4 solution, and the agitation was continued for an additional 10 min. The tightly stoppered bottle containing the Fe $(OH)_3$ gel, which consisted nominally of 0.9 mol dm^{-3} Fe $(OH)_3$, 0.1 mol dm^{-3} Fe^{3+} and 10^{-2} mol dm^{-3} SO_4^{-2}, was placed in an oven preheated to 100°C and the gel was aged for 8 days.

Preparation of hematite/Pt Janus microrobots: The synthesized hematite microparticles were suspended in DI water (5 mg mL^{-1}) and dispersed by sonication. The suspension was dropped by a pipette on glass slides and dried overnight. A 30 nm thin Pt layer was asymmetrically deposited on hematite microparticles by the sputtering method. The real-time thickness of the sputtered Pt layer was controlled by a quartz crystal microbalance. After the sputtering process, microrobots were released using a scalpel.

Microrobots morphological, chemical and structural characterization: Scanning electron microscopy (SEM) images of hematite microparticles and hematite/Pt Janus microrobots were obtained with a Tescan MIRA 3 XMU instrument. For SEM imaging of self-assembled microchains, hematite microrobots were dispersed in DI water, sonicated for 5min. Then, 100 µL of suspended solution was placed on a glass slide under microscope. After hematite microrobots were observed to assemble into microchains, the solution on the glass slide was quickly dried under irradiation of a LED lamp (100 W). Finally, this glass slide moved to the chamber of a Tescan MIRA 3 XMU instrument. Energy-dispersive X-ray spectroscopy (EDX) mapping analysis was performed using an Oxford EDX detector connected to the SEM. The XRD patterns of the products were examined by a Rigaku SmartLab 3 kW diffractometer, equipped with a fine focus Cu sealed tube operating at 40 kV and 30 mA.

Motion experiments: A Nikon ECLIPSE TS2R inverted microscope coupled with a Basler digital camera acA1920-155uc was used to record the microrobots' motion. Briefly, a

microrobot aqueous suspension was dropped on a glass slide. Different concentrations of H_2O_2 (Merck, 30%) were subsequently added to the drop to study microrobot motion in 0, 0.1, and 1% H_2O_2. All experiments were carried out in the absence of surfactants. Then, the microrobots were activated by a 365 nm UV LED (Cool LED pE-100) operated at a measured light intensity of 1.6 W cm^{-2}. Videos were recorded at 20 fps and analyzed to obtain microrobot tracks and calculate their speed through NIS Elements Advanced Research software.

Electrochemical measurements: Tafel experiments were carried out using a customized photoelectrochemical setup with a 365 nm UV LED (700 mA powered LZ4-04UV00, LedEngin Inc.) in the two-electrode configuration with either hematite electrode or Pt electrode as working electrodes and an Ag/AgCl electrode as both the reference and counter electrode. The hematite working electrode was made by dropping 100 µL of a 5 mg mL^{-1} aqueous suspension of walnut-like or cubic hematite microparticles on commercial ITO-covered glass slides (1 x 2 cm^2, Sigma Aldrich, 8–12 Ω sq^{-1}), and overnight drying. Pt working electrode was obtained by sputtering a 30 nm thin Pt layer on an ITO-covered glass slide. Tafel measurements were recorded at a scan rate of 5 mV s^{-1} from -0.2 to 0.6 V *vs.* Ag/AgCl under UV-light irradiation on the working electrodes (1 x 1 cm^2 immersed area) in DI water using a Metrohm AUTOLAB potentiostat.

Numerical simulation

The numerical simulation was performed using the transport of diluted species module of the COMSOL Multiphysics software for the cross-section of two adjacent hematite/Pt Janus

microrobots. Each microrobot was designed as a square with a size of 2 μm x 2 μm. The H_2O generation at the interface between Pt and H_2O_2 due to the photogenerated electron-hole pairs in hematite was simulated. For this purpose, one of the sides of each square was considered as the generation one to emulate the face of the microrobot coated by the Pt layer. The most significant configurations of the two microrobots have been taken into account in the simulation. To calculate the H_2O diffusion for 0.1 s light irradiation, an H_2O diffusion coefficient in water at 25°C of 2.99×10^{-9} m^2 s^{-1} was used, while the photogeneration rate was set to 1 mmol m^{-2} s^{-1}.

Magnetic experiment

Magnetic field-controlled navigation experiments were performed using a homemade magnetic controller system consisting of three orthogonal coil pairs in a 3D-printed polylactic acid (PLA) backbone, which generate a transversal rotating magnetic field. Navigation experiments were performed with an applied magnetic field of 3mT at the frequency of 10 Hz inside a 100 μm wide microfluidic channel. Videos were recorded by using a Nikon ECLIPSE TS2R inverted microscope and Pylon Viewer software at 20 fps.

Yeast cells transport: 5 g of commercial yeast extract was suspended in 200 ml of distilled water under magnetic stirring for 10 min. Then, the solution was moved to an autoclave and heated at 121℃ for 15 min. After that, the broth was vortexed briefly to disperse yeast cells and immediately moved to a temperature-controlled shaking incubator at 300 rpm for 4 h at 37°C. Yeast cells were centrifuged at 5000 rpm for 5 min to remove the culture media and then

transferred in DI water (See the referenced protocol in Supporting Information). An aqueous diluted yeast suspension (5 μL) and a suspension of the cubic hematite microrobots (5 μL, 1 mg mL^{-1}) were placed onto a glass slide to record the videos at a final concentration of 0.1% H_2O_2.

Removal of suspended matter in water: 1 g of commercial toothpaste was dissolved in 200 ml water. Then, a vacuum filtration device was used to filter the solution. A membrane (Whatman membrane filter) with 0.2 μm holes was used. After the filtration, the extracts were washed with distilled water three times. The final products were obtained after drying in a vacuum oven for 5 h. For the removal of suspended matter, 5 μL of the resulting solution (2 mg mL^{-1}), 5 μL cubic hematite microrobots (3 mg mL^{-1}), and 5 μL 0.1% H_2O_2 (the final concentration) were mixed to a clean glass slide to record videos.

PEG photodegradation: The photocatalytic degradation ability of microrobots was evaluated through the degradation of polyethylene glycol (PEG, Mw 4000, Alfa Aesar) under UV-light irradiation. 1 mg of PEG 4000 and 1 mg of microrobots (3 mg mL^{-1}) were added to 1 ml of 1% H_2O_2 solution in a disposable cuvette. The cuvette was irradiated for 24 h using a 365 nm UV LED lamp (9 W) as the light source. Similarly, three control samples were prepared: i) without addition of microrobots; ii) UV-light irradiation without H_2O_2 and microrobots; iii) 1% H_2O_2 without UV-light irradiation and microrobots; After the degradation experiments, all solution were centrifugated at 3500 rpm for 5 min to separate the solution from the microrobots for further analyses. The PEG 4000 degradation was evaluated by UltrafleXtreme Matrix-Assisted

Laser Desorption/Ionization Mass Spectrometry (MALDI-MS, Bruker Daltonics, Bremen, Germany) operated in linear positive detection mode following the protocol of a previous paper.[22]

Associated content

Supporting information:

Normalized XRD patterns of hematite microparticles with walnut-like and cubic shapes; Schematic illustration of the photocatalytic activation and their self-propulsion mechanism; Dipolar moment orientation in a walnut-like hematite microparticle; SEM images after 10 min of observation; SEM and EDX elemental mapping images of rod-shaped and nano-sized cubic hematite particles; Collective behavior of rod-shaped and nano-sized cubic microrobots in pure water in the absence of UV-light irradiation after 5 min observation; Snapshots showing the formation process of self-assembled microchains with time in pure water in the presence and absence of UV-light irradiation; Self-assembly of cubic hematite microparticles in water without light irradiation; Magnetic hysteresis loop of bare hematite microcubes; Optical images showing the behavior of microchains under a transversal rotating magnetic field inside a microfluidic channel; SEM images of suspended matter extracted from a commercial toothpaste; Original time-lapse images of a self-assembled microchain for the removal of suspended matter under UV-light irradiation in 0.1% H_2O_2; MALDI-MS spectra of PEG treated for 24 h under UV-light irradiation and 1% H_2O_2, in 1% H_2O_2 and no UV-light, UV-light irradiation in no H_2O_2.

Supplementary Movie 1. Hematite/Pt microrobots in 0.1% H_2O_2 under UV-light irradiation

Supplementary Movie 2. Collective behaviors of walnut-like and cubic microrobots

Supplementary Movie 3. Self-assembly process of cubic hematite microrobots

Supplementary Movie 4. Different motion modes of cubic hematite microchains under UV-light irradiation in 0.1% H_2O_2

Supplementary Movie 5. Reconfigurable capability of cubic hematite microrobots

Supplementary Movie 6. Interactions of single cubic hematite microrobots and yeast cells under UV-light irradiation in 0.1% H_2O_2

Supplementary Movie 7. Interactions of self-assembled microchains and yeast cells under UV-light irradiation in 0.1% H_2O_2

Supplementary Movie 8. The self-assembled microchain for removal of suspended matter under UV-light irradiation in 0.1% H_2O_2

Authors Contributions

X.P. performed the fabrication of the microrobots, recorded, and analyzed their motion, performed SEM-EDX analysis, Tafel measurements, carried out the cargo transportation experiments, and interpreted the data. M.Ur. designed the experiments, performed the numerical simulation, and contributed to data interpretation. M. Us. contributed to the degradation experiment and analyzed the data. M.P. originated the idea. M.P. and M.Ur. supervised the project. All authors contributed to writing the manuscript.

Acknowledgments

M.P. was supported by Ministry of Education, Youth and Sports (Czech Republic) grant LL2002 under the ERC CZ program. X.P. was supported by the China Scholarship Council (CSC No. 202008320382). M.Ur. acknowledges the financial support by the European Union's Horizon 2020 research and innovation program under the Marie Skłodowska-Curie grant agreement No. 101038066. CzechNanoLab project LM2018110 funded by MEYS CR is gratefully acknowledged for the financial support of the measurements/sample fabrication at CEITEC Nano Research Infrastructure. CIISB, Instruct-CZ Centre of Instruct-ERIC EU consortium, funded by MEYS CR infrastructure project LM2018127, is gratefully acknowledged for the financial support of the measurements at the CEITEC Proteomics Core Facility.

References

[1] Jin, D.; Yu, J.; Yuan, K.; Zhang, L. Mimicking the Structure and Function of Ant Bridges in a Reconfigurable Microswarm for Electronic Applications. *ACS Nano* **2019**, *13*, 5999–6007.

[2] Garattoni, L.; Birattari, M. Autonomous Task Sequencing in a Robot Swarm. *Sci. Robot.* **2018**, *3*, 1–12.

[3] Rubenstein, M.; Cornejo, A.; Nagpal, R. Programmable Self-assembly in a Thousand-robot Swarm. *Science* **2014**, *345*, 795–800.

[4] Soto, F.; Karshalev, E.; Zhang, F.; Avila, B.; Wang, J. Smart Materials for Microrobots. *Chem. Rev.* **2021**.

[5] Wang, H.; Moo, J.; Pumera, M. From Nanomotors to Micromotors: The Influence of the

Size of an Autonomous Bubble-Propelled Device upon Its Motion. *ACS Nano* **2016**, *10*, 5041–5050.

[6] Li, J.; Yu, X.; Xu, M.; Liu, W.; Sandraz, E.; Lan, H.; Wang, J.; Cohen, M. Metal-organic Frameworks as Micromotors with Tunable Engines and Brakes. *J. Am. Chem. Soc.* **2017**, *139*, 611–614.

[7] Wang, Q.; Dong, R.; Wang, C.; Xu, S.; Chen, D.; Liang, Y.; Ren, B.; Gao, W.; Cai, Y. Glucose-Fueled Micromotors with Highly Efficient Visible-Light Photocatalytic Propulsion. *ACS Appl. Mater. Interfaces* **2019**, *11*, 6201−6207.

[8] Ma, X.; Wang, X.; Hahn, K.; Sánchez, S. Motion Control of Urea-Powered Biocompatible Hollow Microcapsules. *ACS Nano* **2016**, *10*, 3597–3605.

[9] Pourrahimi, A. M.; Villa, K.; Palenzuela, C. L.; Ying, Y.; Sofer, Z.; Pumera, M. Catalytic and Light-Driven ZnO/Pt Janus Nano/Micromotors: Switching of Motion Mechanism via Interface Roughness and Defect Tailoring at the Nanoscale. *Adv. Funct. Mater.* **2019**, *29*, 1–8.

[10] Lin, Z.; Fan, X.; Sun, M.; Gao, C.; He, Q.; Xie, H. Magnetically Actuated Peanut Colloid Motors for Cell Manipulation and Patterning. *ACS Nano* **2018**, *12*, 2539–2545.

[11] Xu, T.; Soto, F.; Gao, W.; Garcia-Gradilla, V.; Li, J.; Zhang, X.; Wang, J.; Ultrasound-Modulated Bubble Propulsion of Chemically Powered Microengines. *J. Am. Chem. Soc.* **2014**, *136*, 8552–8555.

[12] Urso, M.; Iffelsberger, C.; Mayorga-Martinez, C. C.; Pumera, M. Nickel Sulfide Microrockets as Self-Propelled Energy Storage Devices to Power Electronic Circuits ‘On-Demand. *Small Methods* **2021**, *2100511*, 1–9.

[13] Oral, C. M.; Ussia, M.; Pumera, M. Self-Propelled Activated Carbon Micromotors for 'on-the-Fly' Capture of Nitroaromatic Explosives. *J. Phys. Chem. C* **2021**, *125*, 18040–18045.

[14] Gao, W.; D'Agostino, M.; Garcia-Gradilla, V.; Orozco, J.; Wang, J. Multi-fuel Driven Janus Micromotors. *Small* **2013**, *9*, 467–471.

[15] Eskandarloo, H.; Kierulf, A.; Abbaspourrad, A. Light-harvesting Synthetic Nano- and Micromotors: A Review. *Nanoscale* **2017**, *9*, 12218–12230.

[16] Jurado-Sánchez, B.; Pacheco, M.; Maria-Hormigos, R.; Escarpa, A. Perspectives on Janus Micromotors: Materials and Applications. *Appl. Mater. Today* **2017**, *9*, 407–418.

[17] Jurado-Sánchez, B.; Pacheco, M.; Rojo, J.; Escarpa, A. Magnetocatalytic Graphene Quantum Dots Janus Micromotors for Bacterial Endotoxin Detection. *Angew. Chemie - Int. Ed.* **2017**, *56*, 6957–6961.

[18] Dong, R.; Zhang, Q.; Gao, W.; Pei, A.; Ren, B. Highly Efficient Light-Driven TiO_2−Au Janus Micromotors. *ACS Nano* **2016**, *10*, 839–844.

[19] Ussia, M.; Urso, M.; Dolezelikova, K.; Michalkova, H.; Adam, V.; Pumera, M. Active Light-Powered Antibiofilm ZnO Micromotors with Chemically Programmable Properties. *Adv. Funct. Mater.* **2021**, *2101178*, 1-10.

[20] Pourrahimi, A. M.; Villa, K.; Ying, Y.; Sofer, Z.; Pumera, M. ZnO/ZnO_2 /Pt Janus Micromotors Propulsion Mode Changes with Size and Interface Structure: Enhanced Nitroaromatic Explosives Degradation under Visible Light. *ACS Appl. Mater. Interfaces* **2018**, *10*, 42688–42697.

[21] Peng, X.; Zhu, H.; Chen, H.; Feng, X.; Liu, R.; Huang, Z.; Shen, Q.; Ma, Y.; Wang, L.

Eco-friendly Porous Iron(iii) Oxide Micromotors for Efficient Wastewater Cleaning. *New J. Chem.* **2019**, *43*, 12594–12600.

[22] Urso, M.; Ussia, M.; Pumera, M. Breaking Polymer Chains with Self-Propelled Light-Controlled Navigable Hematite Microrobots. *Adv. Funct. Mater.* **2021**, *2101510*, 1–10.

[23] Dong, R.; Hu, Y.; Wu, Y.; Gao, W.; Ren, B.; Wang, Q.; Cai, Y. Visible-Light-Driven BiOI-Based Janus Micromotor in Pure Water. *J. Am. Chem. Soc.* **2017**, *139*, 1722–1725.

[24] Xiao, Z.; Chen, J.; Duan, S.; Lv, X.; Wang, J.; Ma, X.; Tang, J.; Wang, W. Bimetallic Coatings Synergistically Enhance the Speeds of Photocatalytic TiO_2 Micromotors. *Chem. Commun.* **2020**, *56*, 4728–4731.

[25] Maric, T.; Nasir, M. Z.; Webster, M. R. D.; Pumera, M. Tailoring Metal/TiO_2 Interface to Influence Motion of Light-Activated Janus Micromotors. *Adv. Funct. Mater.* **2020**, *1908614*, 1–6.

[26] Kong, L.; Rohaizad, N.; Nasir, M.; Guan, J.; Pumera, M. Micromotor-Assisted Human Serum Glucose Biosensing. *Anal. Chem.* **2019**, *91*, 5660–5666.

[27] Gao, W.; Dong, R.; Thamphiwatana, S.; Li, J.; Gao, W.; Zhang, L.; Wang, J. Artificial Micromotors in the Mouse's Stomach: A Step toward in Vivo Use of Synthetic Motors. *ACS Nano* **2015**, *9*, 117–123.

[28] Mayorga-Martinez, C; Zelenka, J.; Grmela, J.; Michalkova, H.; Ruml, T.; Mareš, J.; Pumera, M. Swarming Aqua Sperm Micromotors for Active Bacterial Biofilms Removal in Confined Spaces. *Adv. Sci.* **2021**, *2101301*, 1–7.

[29] Peng, X.; Urso, M.; Pumera, M. Photo-Fenton Degradation of Nitroaromatic Explosives by Light-Powered Hematite Microrobots: When Higher Speed Is Not What We Go For.

Small Methods **2021**, *2100617*, 1–9.

[30] Lu, C.; Tang, Z. Advanced Inorganic Nanoarchitectures from Oriented Self-Assembly. *Adv. Mater.* **2016**, *28*, 1096–1108.

[31] Yan, J.; Bloom, M.; Bae, S. C.; Luijten, E.; Granick, S. Linking Synchronization to Self-assembly Using Magnetic Janus Colloids. *Nature* **2012**, *491*, 578–581.

[32] Yu, J.; Yang, L.; Zhang, L. Pattern Generation and Motion Control of a Vortex-like Paramagnetic Nanoparticle Swarm. *Int. J. Rob. Res.* **2018**, *37*, 912–930.

[33] Snezhko, A.; Aranson, I. S. Magnetic Manipulation of Self-assembled Colloidal Asters. *Nat. Mater.* **2011**, *10*, 698–703.

[34] Breen, T. L.; Tien, J.; Scott, R.; Hadzic, T.; Whitesides, G. M. Design and Self-Assembly of Open, Regular, 3D Mesostructures. *Science* **1999**, *284*, 948−951.

[35] Gobre, V. V.; Tkatchenko, A. Scaling Laws for Van Der Waals Interactions in Nanostructured Materials. *Nat. Commun.* **2013**, *4*, 2341.

[36] Miele, E.; Raj, S.; Baraissov, Z.; Král, P.; Mirsaidov, U. Dynamics of Templated Assembly of Nanoparticle Filaments within Nanochannels. *Adv. Mater.* **2017**, *29*, 1702682.

[37] Villa, K.; Děkanovský, L.; Plutnar, J.; Kosina, J.; Pumera, M. Swarming of Perovskite-Like Bi_2WO_6 Microrobots Destroy Textile Fibers under Visible Light. *Adv. Funct. Mater.* **2020**, *30*, 2007073.

[38] Tottori, S.; Zhang, L.; Peyer, K, E.; Nelson, B. J. Assembly, Disassembly, and Anomalous Propulsion of Microscopic Helices. *Nano Lett.* **2013**, *13*, 4263−4268.

[39] Wang, W.; Castro, L. A.; Hoyos, M.; Mallouk, T. E. Autonomous Motion of Metallic

Microrods Propelled by Ultrasound. *Small* **2015**, *11*, 2836-2846.

[40] Kment, S.; Schmuki, P.; Hubicka, Z.; Machala, L.; Kirchgeorg, R.; Liu, N.; Wang, L.; Lee, K.; Olejnicek, J.; Cada, M.; Gregora, I.; Zboril R. Photoanodes with Fully Controllable Texture: The Enhanced Water Splitting Efficiency of Thin Hematite Films Exhibiting Solely (110) Crystal Orientation. *ACS Nano* **2015**, *9*, 7113-7123.

[41] Zhang, X.; Klaver, P.; Santen, R.; Sanden, M. C.; Bieberle-Hütter, A. Oxygen Evolution at Hematite Surfaces: The Impact of Structure and Oxygen Vacancies on Lowering the Overpotential. *J. Phys. Chem. C* **2016**, *120*, 18201−18208.

[42] Lee, S. H.; Liddell, C. M. Anisotropic Magnetic Colloids: A Strategy to Form Complex Structures Using Nonspherical Building Blocks. *Small* **2010**, *5*, 1957-1962.

[43] Rossi, L.; Donaldson, J.; Meijer, J.; Petukhov, A.; Kleckner, D.; Kantorovich, S.; Irvine, W.; Philipsec, A.; Sacanna, S.; Self-organization in Dipolar Cube Fluids Constrained by Competing Anisotropies. *Soft Matter* **2018**, *14*, 1080–1087.

[44] Meijer J. M.; Rossi, L. Preparation, Properties, and Applications of Magnetic Hematite Microparticles. *Soft Matter* **2021**, *17*, 2354–2368.

[45] Villa, K.; Novotný, F.; Zelenka, J.; Browne, M. P.; Ruml, T.; Pumera, M. Visible-Light-Driven Single-Component $BiVO_4$ Micromotors with the Autonomous Ability for Capturing Microorganisms. *ACS Nano* **2019**, *13*, 8135–8145.

[46] Hong, Y.; Diaz, M.; Cordova-Figueroa, U. M.; Sen, A. Light-Driven Titanium-Dioxide-Based Reversible Microfireworks and Micromotor/Micropump Systems. *Adv. Funct. Mater.* **2010**, *20*, 1568−1576.

[47] Wang, Y.; Zhou, C.; Wang, W.; Xu, D.; Zeng, F.; Zhan, C.; Gu, J.; Li, M.; Zhao, W.;

Zhang, J.; Guo, J.; Feng, H.; Ma, X. Photocatalytically Powered Matchlike Nanomotor for Light-Guided Active SERS Sensing. *Angew. Chem., Int. Ed.* **2018**, *57*, 13110.

[48] Yuan, K.; Pacheco, M.; Jurado-Sánchez, B.; Escarpa, A. Design and Control of the Micromotor Swarm Toward Smart Applications. *Adv. Intell. Syst.* **2021**, *3*, 2100002.

[49] Wang, L.; Kaeppler, A.; Fischer, D.; Simmchen, J. Photocatalytic TiO_2 Micromotors for Removal of Microplastics and Suspended Matter. *ACS Appl. Mater. Interfaces* **2019**, *11*, 32937−32944.Jurado-Sánchez B.; Wang J. Micromotors for Environmental Applications: A Review. *Environ. Sci.: Nano*, **2018**, *5*, 1530−1544.

[50] Jurado-Sánchez B.; Wang J. Micromotors for Environmental Applications: A Review. *Environ. Sci.: Nano*, **2018**, *5*, 1530−1544.

[51] Ussia, M.; Urso, M. Miritello, M.; Bruno, E.; Curcuruto, G.; Vitalini, D.; Condorelli, G.; Cantarella, M.; Priviterab, V.; Carroccio, S. C. Hybrid Nickel-Free Graphene/Porphyrin Rings for Photodegradation of Emerging Pollutants in Water. *RSC Adv.* **2019**, *9*, 30182–30194.

[52] Shahzad, K.; Aeken, W. V.; Mottaghi, M.; Kamyab, V. K.; Kuhn, S. Aggregation and Clogging Phenomena of Rigid Microparticles in Microfluidics. *Microfluidics and Nanofluidics* **2018**, *22*, 1-17.